HHS Public Access

Author manuscript

Traffic. Author manuscript; available in PMC 2024 October 16.

Published in final edited form as:

Traffic. 2024 April ; 25(4): e12933. doi:10.1111/tra.12933.

ATG7(2) Interacts With Metabolic Proteins and Regulates Central Energy Metabolism

Kevin Ostacolo[1], **Adrián López García de Lomana**[2], **Clémence Larat**[1], **Valgerdur Hjaltalin**[1], **Kristrun Yr Holm**[1], **Sigríður S. Hlynsdóttir**[1], **Margaret Soucheray**[3,4,5], **Linda Sooman**[1], **Ottar Rolfsson**[2], **Nevan J. Krogan**[3,4,5], **Eirikur Steingrimsson**[2], **Danielle L. Swaney**[3,4,5], **Margret H. Ogmundsdottir**[1]

[1]Department of Anatomy, Biomedical Center, Faculty of Medicine, University of Iceland, Reykjavik, Iceland

[2]Department of Biochemistry and Molecular Biology, Biomedical Center, Faculty of Medicine, University of Iceland, Reykjavik, Iceland

[3]Gladstone Institutes, San Francisco, California, USA

[4]Department of Cellular and Molecular Pharmacology, University of California, San Francisco, California, USA

[5]Quantitative Biosciences Institute (QBI), University of California, San Francisco, California, USA

Abstract

Macroautophagy/autophagy is an essential catabolic process that targets a wide variety of cellular components including proteins, organelles, and pathogens. ATG7, a protein involved in the autophagy process, plays a crucial role in maintaining cellular homeostasis and can contribute to the development of diseases such as cancer. ATG7 initiates autophagy by facilitating the lipidation of the ATG8 proteins in the growing autophagosome membrane. The noncanonical isoform ATG7(2) is unable to perform ATG8 lipidation; however, its cellular regulation and function are unknown. Here, we uncovered a distinct regulation and function of *ATG7(2)* in contrast with *ATG7(1)*, the canonical isoform. First, affinity-purification mass spectrometry analysis revealed that ATG7(2) establishes direct protein–protein interactions (PPIs) with metabolic proteins, whereas ATG7(1) primarily interacts with autophagy machinery proteins. Furthermore, we identified that ATG7(2) mediates a decrease in metabolic activity, highlighting a novel splice-dependent function of this important autophagy protein. Then, we found a divergent expression pattern of *ATG7(1)* and *ATG7(2)* across human tissues. Conclusively, our work uncovers the divergent patterns of expression, protein interactions, and function of ATG7(2) in contrast to ATG7(1). These findings suggest a molecular switch between main catabolic processes through isoform-dependent expression of a key autophagy gene.

Correspondence: Margret H. Ogmundsdottir (mho@hi.is).

Supporting Information

Additional supporting information can be found online in the Supporting Information section.

Keywords

ATG7; ATG7(2); autophagy; glycolysis; GTEx; isoforms; lipidation; mitochondrial activity; PPI

1 | Introduction

Macroautophagy (hereafter autophagy) is the cell's recycling system [1]. Autophagy plays a major role in organ homeostasis through bulk degradation and selective autophagy, which is important for quality control targeting damaged macromolecules and organelles. This degradation process is an important stress response mechanism providing building blocks for anabolic processes when nutrients are scarce. Autophagy can be nonselective or selective for macromolecules and cellular organelles specifically targeted for degradation. This includes mitophagy which is the selective mitochondrial degradation by autophagy. The dual role of autophagy, as a recycling mechanism and a stress response pathway, is reflected in its connection with cancer. Autophagy can act not only as a tumor suppressor but also as a promoter of tumor growth. Diverse cellular mechanisms are affected by autophagy in tumor cells leading to increased survival under different stress conditions, such as nutrient deprivation and hypoxia. Upregulation of the autophagy process has furthermore been linked with increased chemoresistance [2, 3].

Autophagy starts with the formation of the phagophore, a double membrane that elongates and matures into an autophagosome. This starts with a nucleation step, followed by the elongation of the phagophore membranes involving the lipidation of ATG8 protein family members (LC3/GABARAPs). The final step of the autophagy process is the fusion of the autophagosome with the lysosome to form an autolysosome in which degradation occurs [4].

ATG7 (ubiquitin-like modifier–activating enzyme ATG7) is an E1-like enzyme which acts as a dimer through dimerization of the C-terminal domain [5]. ATG7 is an essential protein for the lipidation of ATG8 protein family members at the growing phagophore. Indeed, after the exposition of the C-terminal glycine residue of ATG8 via ATG4-mediated cleavage, ATG7 mediates the adenylation of ATG8 leading to its conjugation to phosphatidylethanolamine. In parallel, ATG7 adenylates ATG12 which then forms a complex with ATG5 and supports ATG8 lipidation [6].

Three protein coding isoforms represent ATG7 in human tissues: *ATG7(1)*, *ATG7(2)*, and *ATG7(3)*. *ATG7(1)* encodes the longest and canonical isoform with 703 amino acids (aa) and consists of 19 exons, *ATG7(2)* does not contain exon 17 (27 aa), and an isoform termed *ATG7(3)* lacks exons 6 and 18: 39 aa from the N terminus and 41 from the C terminus [7].

We have previously shown that ATG7(2) is unable to interact with ATG8 proteins [7]. This renders ATG7(2) unable to mediate the lipidation of ATG8 proteins, which is the main characterized function of ATG7 [7]. The effect of ATG7 has mainly been attributed to its lipidation activity and thereby autophagy function [6]. However, autophagy-independent functions of ATG7 have been reported [8]. This includes ATG7-mediated repression of proapoptotic properties of caspase-9 and inhibition of proapoptotic genes through interaction with p53 [9, 10].

The importance of ATG7 is reflected in its effects on survival. Atg7-deficient mice cannot survive more than 24 h after birth [11], and *Atg7* ablation in adult mice limits the survival to 3 months [12]. Tissue-specific knockout of Atg7 in the mouse has furthermore highlighted its importance in diverse tissues and cellular mechanisms. *Atg7* knockout in the mouse liver shows multiple cellular abnormalities, deformed mitochondria, hepatomegaly, and tumor formation [11–14]. The importance of Atg7 in metabolic homeostasis is reflected in Atg7 deficiency leading to glycemic and lipid disorders in organs with high metabolic function such as liver [15–17], brain [18, 19], muscle [12, 20], and pancreas [8, 21, 22], causing serious metabolic defects. Nevertheless, the role of ATG7 in metabolic homeostasis remains somewhat unknown.

In this study, we performed mass spectrometry analysis of the protein interactome of ATG7(1) and ATG7(2) to characterize the activity of ATG7(2). This analysis showed that whereas ATG7(1) interacts with autophagy proteins, ATG7(2) lacks this interaction and binds metabolic proteins. Functional experiments revealed altered effects of the two isoforms on metabolic activity. Then, we characterized the expression of *ATG7(2)* in comparison with *ATG7(1)* in human tissues revealing that they do not correlate in expression and have a distinct expression pattern. These results highlight a novel splice-dependent function of this important autophagy protein.

2 | Results

2.1 | ATG7(2) Does Not Interact With Core Autophagy Machinery Proteins

To gain insight on the role of ATG7(2), we cultivated wild-type mouse embryonic fibroblast (MEF) cells in different conditions and observed an increase in endogenous *Atg7* expression at mRNA level under starvation (Figure S1). The increase in *Atg7(1)* (ENSMUST00000032457.17) expression is consistent with previous publications reporting induced autophagy activity in stress conditions [23], and the increased *Atg7(2)* (ENSMUST00000182428.8) expression suggests that this isoform could play a role in stress coping mechanisms.

Next, we established the overexpression of either human ATG7 isoform using two distinct cell models; MEFs with *Atg7* knocked out (MEF-*Atg7*$^{-/-}$) cells, and a human hepatocellular carcinoma cell line (HuH7), based on the importance of ATG7 in liver [11,13,14]. We generated stable doxycycline inducible overexpression cell lines of ATG7(1) or ATG7(2) coupled with a FLAG-tag. An empty vector (EV) cell line was generated as negative control.

First, we looked at the localization of FLAG–ATG7(1) and FLAG–ATG7(2) in the MEF-*Atg7*$^{-/-}$ and HuH7 cells and observed a similar cytoplasmic localization of the two isoforms in both cell lines (Figure S2A). As previously reported [7], MEF-*Atg7*$^{-/-}$ cells showed a lack of LC3B lipidation. The lipidation of LC3B is frequently assessed by the presence of a lower band on immunoblots, opposed to an unlipidated upper band. The lower LC3B band is absent in MEF-*Atg7*$^{-/-}$ cells, and we also observed accumulation of the autophagy protein p62 when compared with wild-type MEFs, indicating defective autophagy. The induced expression of the full-length ATG7(1) isoform rescues both the defective lipidation and accumulation of p62, contrary to ATG7(2), which fails to rescue this phenotype (Figure

S2B,C). We had previously observed that ATG7(2) is not able to lipidate or interact with the ATG8 family member LC3B in MEF-*Atg7*$^{-/-}$ cells [7]. In HuH7 cells, in which ATG7 is endogenously expressed, we observed a decrease of LC3B lipidation in HuH7–ATG7(2) cells in comparison with HuH7–ATG7(1); however, we did not observe a difference in p62 levels with either ATG7 isoform overexpressed (Figure S2D,E). In the HuH7 cells, we analyzed the interaction of ATG7(2) with another ATG8 family member, GABARAP, using co-immunoprecipitation (Co-IP) based on the FLAG-tagged ATG7 followed by a western blot analysis. The results showed a lack of interaction of ATG7(2) with GABARAP, showing that ATG7(2) lacks this ATG8-binding ability also in the presence of endogenous ATG7 expression in the HuH7 cells (Figure S2F). Altogether, the results showed that ATG7(2) is not able to interact with, or to lipidate ATG8 family proteins in the two cell models.

To interrogate the functional role of the short ATG7(2) isoform, we characterized the protein interactome of both ATG7 isoforms. We utilized both cell lines (MEF-*Atg7*$^{-/-}$ and HuH7) to address whether there is a common pattern in protein–protein interaction (PPI) of the isoforms. We performed affinity-purification mass spectrometry (APMS) analysis using FLAG-tagged ATG7(1) or ATG7(2). To provide better context between the detected PPI, we overlayed known interactions from the STRING database [24]. The results showed that in MEF-*Atg7*$^{-/-}$ cells, ATG7(1) interacts with 12 proteins, of which 8 are involved in autophagy, whereas ATG7(2) interacts with 33 proteins, of which 3 are involved in autophagy. The one common protein interaction for the two isoforms is ATG3 (Figure 1A). Similar results were obtained in HuH7 cells wherein 6 out of the 7 proteins that interact with ATG7(1) participate in autophagy, whereas only 2 out of the 17 proteins that interact with ATG7(2) are involved in autophagy. The two isoforms have three common protein interactions which are ATG3, ARFGAP1, and ATG7 (Figure 1C).

These results show that whereas ATG7(1) binds to autophagy machinery proteins, ATG7(2) lacks these interactions in both MEF-*Atg7*$^{-/-}$ and HuH7 cells.

2.2 | ATG7(2) Interacts With Metabolic Proteins

To study the different interactomes of ATG7(1) and ATG7(2), we calculated the fold change between the two isoforms for all their protein interactions. Based on a fold change, we performed Gene Ontology analysis on 29 proteins with significantly higher interaction with ATG7(2) than with ATG7(1) in MEF-*Atg7*$^{-/-}$cells, and 13 proteins in HuH7 cells (Tables S1–S4). As expected, ATG7(1) mainly interacts with autophagy machinery proteins in the two tested cell lines. Interestingly, ATG7(2) does not interact with autophagy proteins but interacts with metabolic proteins including a large majority of mitochondrial membrane proteins in the two tested cell lines (Tables S5 and S6). Indeed, in comparison with ATG7(1), ATG7(2) has gained interaction with the metabolic proteins Tamm41, Afg3l2, Vwa8, Pfkp, Raf1, Yme1l1, Acaa2, Pgam5, Sqrdl, and Hspb1 in MEF-*Atg7*$^{-/-}$ cells (Figure 1B). The pattern is similar in HuH7 cells where ATG7(2) interacts with UMPS, HK2, TMEM126A, FASTKD5, SFXN3, and SLC25A22 (Figure 1D).

Thus, the interactome analysis of the two cell lines revealed that ATG7(2) interacts with metabolic proteins.

2.3 | ATG7(2) Decreases Metabolic Activity

The protein interactome results revealed that ATG7(2) interacts with two key enzymes in glycolysis. ATG7(2) interacts with phosphofructokinase (Pfkp) in MEF-*Atg7*$^{-/-}$ cells and with hexokinase (HK2) in HuH7 cells. To study the potential role of ATG7(2) in glycolysis, we used the MEF-*Atg7*$^{-/-}$ cells that do not express endogenous Atg7. We measured the extracellular acidification rate (ECAR) consisting of the respiratory acidification which occurs through CO_2, and the glycolytic acidification which occurs through lactate. For this, we maintained the MEF-*Atg7*$^{-/-}$ cells, overexpressing ATG7(1) or ATG7(2), in a starvation medium (glucose, pyruvate, and palmitate free) for 1 h before the addition of high concentrations of glucose which restores normal glycolysis activity. Next, we injected oligomycin to shut down oxidative phosphorylation leading to maximal glycolysis capacity. We observed that glycolysis and maximal glycolysis capacity was lower in MEF-*Atg7*$^{-/-}$–ATG7(2) cells in comparison with MEF-*Atg7*$^{-/-}$–ATG7(1) cells. Additionally, it is important to mention that the glycolysis and maximal glycolysis capacity in MEF-*Atg7*$^{-/-}$–ATG7(2) is lower than in the control cells (MEF-*Atg7*$^{-/-}$–EV) and is higher in MEF-*Atg7*$^{-/-}$–ATG7(1) in comparison with the control (Figures 2A,B and S3A–C; Mann–Whitney *U* test; * is $p < 0.05$). The inhibition of autophagy with bafilomycin blocked the effect of ATG7(1) on glycolysis and led to a lower ECAR in MEF-*Atg7*$^{-/-}$–ATG7(2) cells. It appears that there is a synergistic effect between bafilomycin and ATG7(2), leading to a collective reduction in glycolysis (Figures 2C,D and S3D–F; Mann–Whitney *U* test; * is $p < 0.05$).

Additionally, we studied whether the mitochondrial activity was affected by ATG7(2) expression as the protein interactome revealed that ATG7(2) interacts with mitochondrial membrane proteins. We measured basal and maximal respiration by measuring the oxygen consumption rate (OCR). After the measure of the basal OCR, we used oligomycin, an ATP synthase inhibitor (complex V), to reduce mitochondrial respiration; then, we injected carbonyl cyanide-p-trifluoromethoxyphenylhydrazone (FCCP), which disrupts the proton gradient and leads to the maximal OCR. From this approach, we found that the basal OCR was higher in MEF-*Atg7*$^{-/-}$–ATG7(1) cells in comparison with EV and that the maximal OCR was lower in MEF- *Atg7*$^{-/-}$–ATG7(2) cells and higher in MEF-*Atg7*$^{-/-}$–ATG7(1) cells in comparison with EV (Figures 2E and S4A–C; Mann–Whitney *U* test; * is $p < 0.05$). To investigate the autophagy dependence of this effect, we suppressed autophagy activity using bafilomycin and subsequently observed that the overexpression of ATG7(1) resulted in a higher basal OCR compared with the EV. Additionally, the overexpression of ATG7(2) exhibited a lower basal OCR compared with the EV. Similar effect of the isoform expression on the maximal OCR was observed (Figures 2F and S4D–G; Mann–Whitney *U* test; * is $p < 0.05$).

These results suggest that ATG7(2) has a repressor effect in metabolic activity.

2.4 | *ATG7(1)* and *ATG7(2)* Are Not Correlated in Expression

To gain a better understanding of the distinctions between the protein coding isoforms of ATG7, we characterized and analyzed their expression patterns utilizing 4385 samples from 22 tissues in the Genotype-Tissue Expression (GTEx) database. We found that *ATG7(1)* is the highest expressed isoform representing 84% of total protein coding isoform expression,

ATG7(2) represents 15%, and *ATG7(3)* is barely expressed in human tissues (Figure 3A,B). From these observations, we decided to exclude *ATG7(3)* from our subsequent analysis and focus on characterizing the expression of the canonical isoform, *ATG7(1)*, and the nonlipidating isoform, *ATG7(2)*.

It is of interest, considering the importance of *ATG7*, that its expression is low across human tissues. Indeed, the maximal expression mean is 11 transcripts per million (TPM) in nerve for *ATG7(1)* and is 4 TPM in blood for *ATG7(2)*. Furthermore, the expression level of each isoform is comparable across the different tissues (Figure 3C). Additionally, we evaluated the relative difference in expression of the two main isoforms of *ATG7* in the different tissues. We found that the difference in expression is tissue dependent. In comparison to the other isoform, *ATG7(2)* displays higher relative expression in blood, whereas *ATG7(1)* exhibits the highest relative expression in nerve tissue. However, no significant differences in expression levels were observed between the two isoforms in several tissues, such as breast (Figure 3D–F; Student *t*-test with Bonferroni correction; * is $p < 0.05$).

Next, we analyzed whether the two isoforms correlate in expression. Interestingly, we did not observe a significant correlation in expression of *ATG7(1)* and *ATG7(2)* when analyzing the expression level in all tissues (Figure 3G; Spearman correlation coefficient; $R = 0.004$). We analyzed the correlation of the two isoforms for each tissue and observed that despite significant *p*-value, no tissue had an *R*-value crossing our threshold of 0.6 or $R < -0.6$. In fact, the highest correlation score was for salivary gland with a correlation score of −0.49 (Figure 3H; Spearman correlation coefficient with Bonferroni correction; * is $p < 0.05$). We thus conclude that the two isoforms do not cor relate in expression.

Altogether, these results showed that *ATG7(1)* and *ATG7(2)* are differently expressed across human tissues and are not correlated in expression.

2.5 | *ATG7(1)* and *ATG7(2)* Expression Pattern Diverge Across Human Tissues

Given the lack of expression correlation between the two isoforms across tissues, we sought to understand the expression patterns of *ATG7(1)* and *ATG7(2)* in the context of the whole transcriptome. Therefore, we applied Leiden clustering (Scanpy implementation of Leiden algorithm) on the already mentioned dataset of 4385 whole transcriptome profiles across 22 different tissues from GTEx to identify sets of coexpressed transcripts (see Section 4 for details). We identified an optimal partition of 168 different clusters with a divergent pattern of expression (Figure 4A). We found that *ATG7(1)* and *ATG7(2)* belong to two distinct expression clusters, indicative of a differential expression pattern for these two isoforms across tissues (Figure 4B). Indeed, ATG7(1) and ATG7(2) belong to different clusters in all clustering partitions we explored through varying algorithm parameters (Leiden) that resulted in clustering partitions ranging from 16 to 509 clusters (Figure S5). Furthermore, we visualized the expression pattern of *ATG7(1)* and *ATG7(2)* containing clusters across human tissue. We identified a divergent expression pattern in some tissues, suggesting differential regulation in particular tissues (Figure 4C).

Altogether, our results indicate that collectively within a broader expression program, *ATG7(1)* and *ATG7(2)* have a distinct divergent expression pattern across human tissue.

2.6 | ATG7(2) Has a Unique Secondary Structure

We studied the structural shape of the isoforms using COTHreader (COTH) [25] to know if the different protein interactions for the two isoforms of ATG7 are due to their structure. Based on previous observations about ATG7 dimerization [26], we built the potential human heterodimerization and homodimerization models of ATG7(1) and ATG7(2). The results revealed that dimerization could potentially exist as the missing part of ATG7(2) does not compromise the formation of the dimerization interface. Nevertheless, the 27 aa lacking in ATG7(2) are close to the dimerization interface in the ATG7(1) homodimer and some of them are involved in intermolecular contacts. Therefore, the absence of these aa could potentially affect the dimer stability in an ATG7(2) homodimer or in the heterodimer. In addition, these results showed that the three constructs form a similar bird-like quaternary structure. Using Phyre2 [27], we built the secondary and tertiary structures of ATG7(1) and ATG7(2). We observed that their topology differs to some extent (Figure 5A,B, Figure S6). To investigate this further, we annotated the alpha helices and beta sheets of the secondary structure of each isoform on their aa sequence and aligned them. This approach revealed that ATG7(1) and ATG7(2) secondary structure diverges in the C-terminal region of the protein. Mainly, exon 17 and the surrounding region show a difference in the number, type, and size of secondary structures (Figure 5C). Based on these predictions, we decided to study homodimerization *in vitro*. For that, we used disuccinimidyl suberate (DSS) to cross-link protein complexes in samples from MEF-*Atg7*$^{-/-}$, with overexpression of either human ATG7 isoform. The cell lysates were used for western blot analysis and showed that the ATG7(1) and ATG7(2) form dimers (Figure 5D).

These observations indicate that ATG7(2) is able to form a dimer despite the lack of exon 17. The structure of ATG7(1) and ATG7(2) differs in diverse regions of the protein, which could explain the loss in binding with autophagy machinery proteins for ATG7(2). Moreover, this suggests that ATG7(2) could gain affinity of binding with other molecules.

3 | Discussion

In this study, we characterized the expression and demonstrated a metabolic role of the ATG7(2) isoform of ATG7 that does not have the characterized lipidation function. We found that this isoform represents a minority population of ATG7 (~20%), with highest expression in the blood, whereas the long canonical *ATG7(1)* isoform is expressed more uniformly across tissue types. Interestingly, we found that the two expressed isoforms do not correlate in expression, suggesting that the two isoforms are differently regulated and may have distinct functions. Furthermore, in line with our previous publication, where we showed that *ATG7(2)* could have a significant role in stress conditions [7], we found that endogenous Atg7 isoforms have increased mRNA expression under starvation in MEF cells.

Previously, we observed based on yeast ATG7 protein crystallization bound to ATG8 [28] that the exon lacking in ATG7(2) contains aa required for the binding of ATG7 to ATG8. Based on this observation, we showed that ATG7(2) does not interact with the ATG8 family protein LC3B and is unable to lipidate ATG8 family members [7]. Here, we performed mass spectrometry analysis of the protein interactome of ATG7(1) in comparison with the interactome of ATG7(2) in two different cell lines, HuH7 and MEF-*Atg7*$^{-/-}$ cells. We

found that the canonical ATG7(1) protein binds the autophagy machinery as expected. Interestingly, we found that ATG7(2) does not bind ATG8 proteins or other proteins in the autophagy machinery. We observed reduced or absent binding of ATG7(2) to ATG3, ATG10, and ATG12. The structure of ATG7 and ATG12 has not been resolved and several hypotheses can explain the loss of binding with ATG7(2). It is possible that the required binding sites reside within the exon lacking in ATG7(2) or the first interactions with ATG8 and ATG12 are required for the binding of ATG7 to other proteins in the later steps in the conjugation pathway.

The ATG7 dimer structure in yeast and the predicted structure in human are similar, with both forming a bird-like structure [7,29]. Here, we showed that ATG7(1) and ATG7(2) form homodimers, and the structure models indicate a potential ATG7(1) and ATG7(2) heterodimerization. It has been shown that ATG7(1) interacts with autophagy machinery proteins as a dimer [28,30]. We observed that the overexpression of ATG7(2) in HuH7 cells affects autophagy activity with a decreased LC3B lipidation. One hypothesis could be that ATG7(2) forms heterodimer with the endogenous ATG7(1), blocking its activity. Further biochemical and functional analyses of isoform homodimers and heterodimers will be important for dissecting out the physiological importance of the isoform expression in diverse tissues and diseased states.

The mass spectrometry data further revealed that ATG7(2) interacts with mitochondrial membrane and metabolic proteins. This was observed in both cell types, although the individual metabolic proteins differed. There are three key regulatory enzymes in glycolysis: HK, PFK, and pyruvate kinase (PK) [31]. The interactome showed binding of ATG7(2) to two of these regulatory enzymes: HK2 and PFKP. Functional experiments further showed that MEF-$Atg7^{-/-}$ cells expressing ATG7(2) have a decreased glycolysis rate compared with control cells and cells expressing the ATG7(1) isoform. This is in concert with previous work describing an effect of ATG7 expression on metabolism and particularly an inhibitory effect on glycolysis [15,18,32–35]. Of specific relevance to our findings, ATG7 has previously been reported to interact with PKM2, the third key rate limiting enzyme in glycolysis, resulting in decreased glycolytic activity [36]. Interestingly, this study was performed with an ATG7 construct [37] that we have found to be ATG7(2) [7]. These findings are in line with our observation that ATG7(2) interacts with key regulatory glycolytic enzymes to dampen glycolytic flux.

In addition, we found a significant decrease in ECAR in MEF-$Atg7^{-/-}$ cells expressing only ATG7(2) as well as when subjected to bafilomycin treatment. This outcome was unexpected, considering our prior demonstration that ATG7(2) is incapable of facilitating autophagosome maturation. One possible explanation for this observation could be an upregulation of ATG7(2) expression induced by the stress from bafilomycin treatment. Additional experiments will be important to analyze this further.

The combined rate of extracellular acidification consists of two parts, namely respiratory acidification, which occurs through CO_2, and glycolytic acidification, which occurs through lactate. Lactate contributes to tumor development and growth, acting as an interchangeable metabolite in the tumor environment [38]. It would be intriguing to isolate tissues from the

main metabolic organs of mouse models and, under various stress conditions, quantify both the endogenous expression of the Atg7(2) protein and the metabolic activity. These findings will be important to characterize further and analyze the metabolic role of ATG7(2) in a tumor context.

The binding of ATG7(2) to glycolysis proteins may sequester their function directly or indirectly, leading to the observed decrease in glycolysis flux. Interestingly, ATG7(2) can interact with the three key enzymes of glycolysis. It has been shown that by direct interaction, ATG7 inhibits PKM2 phosphorylation in MEF cells [36], and this may also apply to inhibitory effects of other glycolytic proteins. Another possibility could be that ATG7(2) mediates degradation of glycolytic proteins and thus leads to decreased glycolytic activity. Interestingly, HK2 has been shown to be degraded through chaperone-mediated autophagy [39]. It is also of interest that ATG7(2) gains binding to an E3–ubiquitin ligase (RLIM) and heat-shock proteins (HSPB1, HSPA1A), indicating a potential role in directing cargo to the ubiquitination and proteasome machinery.

Previous findings on the impact of Atg7 on metabolism in mouse models align with our results in diverse contexts. In neurons, Atg7 deficiency leads to increased body weight, adiposity, and glucose intolerance [18], whereas cardiomyocyte-specific Atg7 depletion results in mitochondrial dysfunction and lipid accumulation [32]. In chronic myeloid leukemia, ATG7 knockdown results in decreased glycolysis and increased oxidative phosphorylation [34]. Deletion of Atg7 in hepatocytes leads to liver enlargement, elevated total cholesterol, and increased levels of triglycerides and lipid droplet–associated proteins [15]. Altogether, our results suggest a role of ATG7(2) in the effects that have been observed for ATG7 on central energy metabolism.

Our results show that an ATG7 isoform expression switch is important for controlling the interplay of the diverse catabolic pathways of autophagy and metabolism. This raises questions as to how the isoform expression is regulated. Alternative splicing is emerging as an important factor in autophagy regulation through different autophagy protein isoforms [40]. An mRNA *ATG7* isoform with an extended 3′ end, but resulting in ATG7(1) protein expression, is regulated by the splicing factor U2AF1 [41]. Characterizing which splicing factors are involved in ATG7(2) splicing will be important to unravel. It is likely that environmental factors have an impact on the differential splicing of ATG7(1) and ATG7(2), resulting in increased autophagy or decreased metabolic activity. Having a better understanding of the molecular mechanisms of ATG7 will help shed light on the complex interplay of autophagy and diverse cellular pathways in healthy and diseased tissues.

4 | Methods

4.1 | RNA-Seq Data Analysis

RNA-seq data were downloaded from Xena Browser data hubs [42] including 7429 samples from GTEx. After selection of the tissues represented by at least 20 samples, we selected 4385 samples by quality control based on the distribution of the gene expression for each sample. Then, we filtered the unexpressed transcripts using quantile normalization to normalize the transcript expression (n = 46 490).

Codes can be found at https://github.com/Keviosta/Article_short_isoform_ATG7.

4.2 | Statistical Analysis

All experiments were performed in at least three independent experiments. Student *t*-test or Mann–Whitney *U* test were used to compare two groups. Welch's *t*-test was used for qPCR analysis. Spearman and Pearson correlation coefficients were used for correlation analysis. $p < 0.05$ was considered statistically significant.

4.3 | Structural Analysis

We collected the aa FASTA sequence of ATG7(1) (ENST00000354449.7) and of ATG7(2) (ENST00000354956.9) and ran the sequences through the COTH platform [25] to predict the potential dimerization of ATG7 isoforms. COTH is a threading algorithm that assembles protein complex structures using templates from both tertiary and complex structure libraries. For each dimer, the model with the highest *Z*-score was selected. The tertiary structure of each monomer was predicted using Phyre2 platform [27]. Pictures of the dimers were created using the PyMOL Molecular Graphics System. ATG7(1) homodimerization; $Z = 6.161$. ATG7(2) homodimerization; $Z = 6.094$. Heterodimerization of ATG7(1) and ATG7(2); $Z = 6.100$.

4.4 | Cell Culture

Two cell lines were used: embryonic fibroblasts from *Atg7* knockout mice (MEF-*Atg7*$^{-/-}$, kindly provided by Dr. Masaaki Komatsu) and the human liver cancer cell line HuH7. To obtain overexpression of *ATG7* isoforms, the two cell lines were generated as described previously in [7]. All cell lines were cultured at 37°C and 5% CO_2 in DMEM +GlutaMAX (Gibco, 31966–021) medium supplemented with 10% fetal bovine serum (Gibco, 10270–106) and kept under G418 (Gibco, 10131–019) selection. Cells were used at 90% confluency for experiments. For each experiment, expression of *ATG7* isoforms was induced with doxycycline (Selleckchem, S4163) in a concentration range from 0.5 to 10 μg/mL for 24 h. Then, for experiments including bafilomycin treatment, culture medium was renewed, and cells received a 100 nM bafilomycin treatment (Sigma, B1793–2UG) or vehicle control (DMSO) for 4 h.

4.5 | Quantitative Real-Time PCR

To quantify Atg7 mRNA expression in MEF cells, we cultivated them for 5 h in nutrient-rich medium (DMEM + GlutaMAX; Gibco, 31966–021) or nutrient-starvation medium (DMEM; Gibco, A1443001) which does not contain glucose and glutamine. Total RNA was extracted from cells using the Quick-RNA Miniprep Kit (Zymo Research R1055) following the manufacturer's protocol. RNA samples were diluted to a final concentration of 100 ng·μL^{-1} in nuclease-free water. Reverse transcription was performed using the High-Capacity cDNA Reverse Transcription Kit (Applied Biosystems no. 4368814) following the manufacturer's protocol for 10 μL reaction volume. cDNA samples were diluted 1:50 in nuclease-free water. qPCR was performed using Luna Universal qPCR Master Mix (New England Biolabs Inc., #M3003) following the manufacturer's protocol for 10 μL reaction volume with 4 μL of

cDNA. The data were normalized to actin mRNA. The following primers were used at a final concentration of 0.25 μM:

Actin:	5′-CATTGCTGACAGGATGCAGAAGG-3′
	5′-TGCTGGAAGGTGGACAGTGAGG-3′
Atg7:	5′-ACCCAGAAGAAGTTGAACGA-3′
	5′-CTCATTTGCTGACTGCTCCA-3′
Atg7(1):	5′-AGCAGTGATGACCGCATGAA-3′
	5′-CCAGGCTGACAGGAAGAACA-3′
Atg7(2):	5′-GCATCCTGAGGGGGGCTACG-3′
	5′-GATCAAGAACCTGGTGAGGCA-3′

4.6 | Dimerization Assay in Cells

To perform the dimerization assay on MEF-$Atg7^{-/-}$ cells, we extracted the proteins with RIPA buffer 1x (Abcam, ab156034) and cross-linked the protein complexes with DSS (Thermo Fisher Scientific, 21555; 50 mM in DMSO) for 30 min at 30°C. The reaction was quenched in 1 M Tris pH 7.4 for 15 min at 30°C. Then, we desalted the proteins using Zeba Spin Desalting Columns (Thermo Fisher Scientific, 89882). Samples were used for western blot analysis.

4.7 | Co-IP for Western Blot

Co-IP was based on the FLAG-tagged ATG7 on the two cell lines. To study the ATG7(1) and ATG7(2) interaction with GABARAP in western blot, we used FLAG Immunoprecipitation Kit (Merck, FLAGIPT1–1KT) following the manufacturer's protocol.

4.8 | Affinity Purification

Cell pellets were lysed with 300 μL of ice-cold lysis buffer (50 mM Tris pH 7.4, 150 mM NaCl, 1 mM EDTA, 0.5% NP40, 1 mM DTT, 1× protease inhibitor cocktail [Roche, complete mini EDTA free], 125 U Benzonase/mL). Lysate was flash-frozen on dry ice for 5–10 min, followed by a 30–45 s thaw in 37°C water bath with agitation, and rotation at 4°C for 15 min. Lysate was clarified by centrifugation at 13 000×*g* for 15 min at 4°C. For FLAG purification, 25 μL of bead slurry (Sigma, Anti-Flag M2 Magnetic Beads) was washed twice with 1 mL of ice-cold wash buffer (50 mM Tris pH 7.4, 150 mM NaCl, 1 mM EDTA), and the lysate was incubated with the anti-FLAG beads at 4°C with rotation for 2 h. After incubation, the flow-through was removed, and beads were washed once with 500 μL of wash buffer with 0.05% NP40 and twice with 1 mL of wash buffer (no NP40). Bound proteins were eluted by incubating beads with 15 μL of 100 μg/mL 3× FLAG peptide in 0.05% RapiGest in wash buffer for 15 min at room temperature (RT) with shaking. Supernatants were removed and elution was repeated. Eluates were combined, and 10 μL of 8 M urea, 250 mM Tris, and 5 mM DTT (final concentration ~1.7 M urea, 50 mM Tris, and 1 mM DTT) were added to give a final total volume of ~45 μL. Samples were incubated at 60°C for 15 min and allowed to cool to RT. Iodoacetamide was added to a final concentration of 3 mM and incubated at RT for 45 min in the dark. DTT was added to a

final concentration of 3 mM before adding 1 μg of sequencing-grade trypsin (Promega) and incubating at 37°C overnight. Samples were acidified to 0.5% TFA (pH < 2) with 10% TFA stock and incubated for 30 min before desalting on C18 stage tip (Rainin).

4.9 | Mass Spectrometry Data Acquisition and Analysis

Samples were resuspended in 15 μL of MS loading buffer (4% formic acid, 2% acetonitrile), and 2 μL was separated by a reversed-phase gradient over a nanoflow 75 μm ID × 25 cm long picotip column packed with 1.9 μM C18 particles (Dr. Maisch). Peptides were directly injected over the course of a 75-min acquisition into a Q-Exactive Plus mass spectrometer (Thermo Fisher Scientific). Raw MS data were searched against the uniprot canonical isoforms of the human proteome (HuH7 cells) or the mouse proteome (MEF cells) and using the default settings in MaxQuant [43] (version 1.5.7.4), with a match-between-runs enabled. Peptides and proteins were filtered to 1% false discovery rate in MaxQuant, and identified proteins were then subjected to PPI scoring. To quantify changes in interactions between isoforms, we used a label-free quantification approach in which statistical analysis was performed using MSstats [44]. All raw data files and search results are available from the PRIDE partner ProteomeXchange repository under the PXD040548 identifier [45,46]. We used Cytoscape to represent the interactions [47] and added the STRING interactions [24] from human for HuH7 cells and from mice for MEF cells.

4.10 | Western Blot

Samples were boiled for 5 min at 95°C. Proteins were separated by SDS–polyacrylamide gel electrophoresis (SDS-PAGE) at 100 V on 12% acrylamide gels. Then, the proteins were transferred onto PVDF membranes (Thermo Fisher Scientific, 88520) at 22 V overnight. Membranes were blocked in 5% BSA (Sigma, A9647) in TBS with 0.1% Tween-20 (Sigma, P1379) for 1 h at RT. Primary antibodies, such as anti-actin (Millipore, MAB1501), anti-FLAG (Sigma, F3165), anti-LC3B (Cell Signaling Technology, #2775), anti-p62 (Cell Signaling Technology, #5114), and anti-GABARAP (Cell Signaling Technology, #E1J4E), were incubated overnight. Finally, DyLight 800 anti-mouse and DyLight 680 anti-rabbit (Cell Signaling Technology) were applied for 1 h at RT. All the antibodies were used at the dilutions recommended by manufacturers. Odyssey imaging system and Image Studio version 2.0 (LI-COR Biosciences) were used to scan the blots.

4.11 | Immunofluorescence Staining and Confocal Microscopy

Cells were seeded onto 12-well glass slides at a density of 1×10^4 cells per well. Then the cells were fixed with 4% paraformaldehyde for 15 min, washed, and incubated for 1 h in blocking buffer. After the washing steps, the primary antibody used was anti-FLAG (Sigma, F3165; 1:5000) with overnight incubation. Then, incubation for 2 h of the secondary antibodies that were Alexa Fluor 546 anti-mouse IgG in HuH7 cell line and Alexa Fluor 647 anti-mouse IgG in MEF cell line (Life Technologies). The slides were mounted with Fluoromount-GTM with DAPI (Invitrogen). Images were captured on a confocal microscope (Olympus FLV1200).

4.12 | Seahorse

Seahorse XFe-96 metabolic extracellular flux analyzer (Seahorse Biosciences, North Billerica, MA, USA) was used to measure ECAR and OCR. MEF-*Atg7*$^{-/-}$ cells were seeded at 3.5 × 10^4 cells per well in a 96-well XF cell culture microplate. Each condition was repeated in sextuplicate.

4.12.1 | Extracellular Acidification Rate—One hour before the assays, medium was changed to DMEM medium pH 7.4 (Seahorse XF Agilent, 103575–100) supplemented with 1× GlutaMax (Gibco, 13462629). Then the cell plate was in a CO_2-free incubator for 1 h before the assay for degassing. At 24 h prior to the assay, the XFe-96 sensor cartridge (Agilent Seahorse) was hydrated in a CO_2-free incubator in the Agilent Seahorse XF Calibrant (Agilent, 100840–000). Before assays, inhibitors were added to the XFe-96 sensor cartridge: glucose (Sigma, G7021; 1 mM), oligomycin (Abcam, ab141829; 1 μM), and 2-deoxy-d-glucose (Sigma, D6134; 1 mM).

4.12.2 | Oxygen Consumption Rate—One hour before the assays, medium was changed to DMEM medium pH 7.4 (Seahorse XF Agilent, 103575–100) supplemented with 1× GlutaMax (Gibco, 13462629), 100 mM pyruvate solution (Seahorse XF Agilent, 103578–100), and 25 mM D-(+)-Glucose (Sigma, G7021). Then the cell plate was placed in a CO_2-free incubator for 1 h before the assay for degassing. At 24 h prior to the assay, the XFe-96 sensor cartridge (Agilent Seahorse) was hydrated in a CO_2-free incubator in the Agilent Seahorse XF Calibrant (Agilent, 100840–000). Before assays, inhibitors were added to the XFe-96 sensor cartridge: oligomycin (Abcam, ab141829; 1 μM), FCCP (Sigma, C2920; 1.2 μM), and a mixture of rotenone (Sigma, 557368; 1 mM) and antimycin A (Sigma, 1397–94-0; 1 mM).

During assays, seven measurements for baseline and three measurements after the addition of each metabolic inhibitor were performed. Each measure consists of mixing for 3 min and measuring for 3 min. At the end of the assays, values were normalized on cell number. The number of cells was calculated from protein quantification using BCA Protein Assay Kit (Thermo Fisher Scientific, 23225).

Supplementary Material

Refer to Web version on PubMed Central for supplementary material.

Acknowledgments

This work was supported by Icelandic Research Fund grants (Grants 184727-051, 228586-051, and 207307-051), and Icelandic Cancer Society Research Fund grant. The work was also supported by National Institutes of Health funding (NIH U54 CA209891) to NJK. We thank Masaaki Komatsu for generously providing us with the MEF-*Atg7*$^{-/-}$ cells. We also thank Vivian Pogenberg for critical comments on the manuscript.

Funding:

This work was supported by Icelandic Research Fund grants (Grants 184727-051, 228586-051, and 207307-051), Icelandic Cancer Society Research Fund grant and National Institutes of Health funding U54 CA209891.

Conflicts of Interest

The N.J.K. laboratory has received research support from Vir Biotechnology, F. Hoffmann-La Roche, and Rezo Therapeutics. N.J.K. has financially compensated consulting agreements with the Icahn School of Medicine at Mount Sinai, New York, Maze Therapeutics, Interline Therapeutics, Rezo Therapeutics, GEn1E Lifesciences Inc., and Twist Bioscience Corp. He is on the Board of Directors of Rezo Therapeutics and is a shareholder in Tenaya Therapeutics, Maze Therapeutics, Rezo Therapeutics, and Interline Therapeutics. D.L.S. has a consulting agreement with Maze Therapeutics and Rezo Therapeutics.

Abbreviations:

aa	amino acids
APMS	affinity-purification mass spectrometry
Co-IP	co-immunoprecipitation
ECAR	extracellular acidification rate
EV	empty vector
GTEx	Genotype-Tissue Expression
HuH7	human hepatocellular carcinoma
MEF-*Atg7*$^{-/-}$	mouse embryonic fibroblasts with *Atg7* knocked out
PPI	protein–protein interaction
TPM	transcripts per million

References

1. Galluzzi L, Baehrecke EH, Ballabio A, et al. , “Molecular Definitions of Autophagy and Related Processes,” The EMBO Journal 36, no. 13 (2017): 1811–1836, 10.15252/embj.201796697. [PubMed: 28596378]
2. Li X, He S, and Ma B, “Autophagy and Autophagy-Related Proteins in Cancer,” Molecular Cancer 19, no. 1 (2020): 12, 10.1186/s12943-020-1138-4. [PubMed: 31969156]
3. Levy JMM, Towers CG, and Thorburn A, “Targeting Autophagy in Cancer,” Nature Reviews Cancer 17, no. 9 (2017): 528–542, 10.1038/nrc.2017.53. [PubMed: 28751651]
4. Kawabata T and Yoshimori T, “Beyond Starvation: An Update on the Autophagic Machinery and Its Functions,” Journal of Molecular and Cellular Cardiology 95 (June 2016): 2–10, 10.1016/j.yjmcc.2015.12.005. [PubMed: 26682507]
5. Isei Tanida ET-M, Ueno T, and Kominami E, “The Human Homolog of Saccharomyces cerevisiae Apg7p Is a Protein-Activating Enzyme for Multiple Substrates Including Human Apg12p, GATE-16, GABARAP, and MAP-LC3,” Journal of Biological Chemistry 276 (2001): 1701–1706. [PubMed: 11096062]
6. Collier JJ, Suomi F, Oláhová M, McWilliams TG, and Taylor RW, “Emerging Roles of ATG7 in Human Health and Disease,” EMBO Molecular Medicine 13, no. 12 (2021): e14824, 10.15252/emmm.202114824. [PubMed: 34725936]
7. Ogmundsdottir MH, Fock V, Sooman L, et al. , “A Short Isoform of ATG7 Fails to Lipidate LC3/GABARAP,” Scientific Reports 8, no. 1 (2018): 14391, 10.1038/s41598-018-32694-7. [PubMed: 30258106]
8. Long JS, Kania E, McEwan DG, et al. , “ATG7 Is a Haploinsufficient Repressor of Tumor Progression and Promoter of Metastasis,” Proceedings of the National Academy of Sciences of the

United States of America 119, no. 28 (2022): e2113465119, 10.1073/pnas.2113465119. [PubMed: 35867735]

9. Lee IH, Kawai Y, Fergusson MM, et al. , "Atg7 Modulates p53 Activity to Regulate Cell Cycle and Survival During Metabolic Stress," Science 336, no. 6078 (2012): 225–228, 10.1126/science.1218395. [PubMed: 22499945]
10. Han J, Hou W, Goldstein LA, Stolz DB, Watkins SC, and Rabinowich H, "A Complex Between Atg7 and Caspase-9," Journal of Biological Chemistry 289, no. 10 (2014): 6485–6497, 10.1074/jbc.m113.536854. [PubMed: 24362031]
11. Komatsu M, Waguri S, Ueno T, et al. , "Impairment of Starvation-Induced and Constitutive Autophagy in Atg7-Deficient Mice," The Journal of Cell Biology 169, no. 3 (May 2005): 425–434, 10.1083/jcb.200412022. [PubMed: 15866887]
12. Karsli-Uzunbas G, Guo JY, Price S, et al. , "Autophagy Is Required for Glucose Homeostasis and Lung Tumor Maintenance," Cancer Discovery 4, no. 8 (August 2014): 914–927, 10.1158/2159-8290.cd-14-0363. [PubMed: 24875857]
13. Takamura A, Komatsu M, Hara T, et al. , "Autophagy-Deficient Mice Develop Multiple Liver Tumors," Genes & Development 25, no. 8 (April 2011): 795–800, 10.1101/gad.2016211. [PubMed: 21498569]
14. Lee YA, Noon LA, Akat KM, et al. , "Autophagy Is a Gatekeeper of Hepatic Differentiation and Carcinogenesis by Controlling the Degradation of Yap," Nature Communications 9, no. 1 (2018): 4962, 10.1038/s41467-018-07338-z.
15. Singh R, Kaushik S, Wang Y, et al. , "Autophagy Regulates Lipid Metabolism," Nature 458, no. 7242 (2009): 1131–1135, 10.1038/nature07976. [PubMed: 19339967]
16. Allaire M, Rautou PE, Codogno P, and Lotersztajn S, "Autophagy in Liver Diseases: Time for Translation?" Journal of Hepatology 70 (January 2019): 985–998, 10.1016/j.jhep.2019.01.026. [PubMed: 30711404]
17. Baselli GA, Jamialahmadi O, Pelusi S, et al. , "Rare ATG7 Genetic Variants Predispose Patients to Severe Fatty Liver Disease," Journal of Hepatology 77, no. 3 (2022): 596–606, 10.1016/j.jhep.2022.03.031. [PubMed: 35405176]
18. Coupé B, Ishii Y, Dietrich MO, Komatsu M, Horvath TL, and Bouret SG, "Loss of Autophagy in Pro-Opiomelanocortin Neurons Perturbs Axon Growth and Causes Metabolic Dysregulation," Cell Metabolism 15, no. 2 (2012): 247–255, 10.1016/j.cmet.2011.12.016. [PubMed: 22285542]
19. Kaushik S, Arias E, Kwon H, et al. , "Loss of Autophagy in Hypothalamic POMC Neurons Impairs Lipolysis," EMBO Reports 13, no. 3 (2012): 258–265, 10.1038/embor.2011.260. [PubMed: 22249165]
20. Masiero E, Agatea L, Mammucari C, et al. , "Autophagy Is Required to Maintain Muscle Mass," Cell Metabolism 10, no. 6 (2009): 507–515, 10.1016/j.cmet.2009.10.008. [PubMed: 19945408]
21. Zhou X, Xie L, Xia L, et al. , "RIP3 Attenuates the Pancreatic Damage Induced by Deletion of ATG7," Cell Death & Disease 8, no. 7 (2017): e2918, 10.1038/cddis.2017.313. [PubMed: 28703808]
22. Xia L, Xu Z, Zhou X, et al. , "Impaired Autophagy Increases Susceptibility to Endotoxin-Induced Chronic Pancreatitis," Cell Death & Disease 11, no. 10 (2020): 889, 10.1038/s41419-020-03050-3. [PubMed: 33087696]
23. Klionsky DJ, Abdel-Aziz AK, Abdelfatah S, et al. , "Guidelines for the Use and Interpretation of Assays for Monitoring Autophagy (4th Edition)," Autophagy 17, no. 1 (2021): 1–382, 10.1080/15548627.2020.1797280. [PubMed: 33634751]
24. Damian Szklarczyk ALG, Nastou KC, Lyon D, et al. , "The STRING Database in 2021: Customizable Protein–Protein Networks, and Functional Characterization of User-Uploaded Gene/Measurement Sets," Nucleic Acids Research 49 (2021): 10800. [PubMed: 34530444]
25. Mukherjee S and Zhang Y, "Protein-Protein Complex Structure Predictions by Multimeric Threading and Template Recombination," Structure 19, no. 7 (2011): 955–966, 10.1016/j.str.2011.04.006. [PubMed: 21742262]
26. Komatsu M, Tanida I, Ueno T, Ohsumi M, Ohsumi Y, and Kominami E, "The C-terminal Region of an Apg7p/Cvt2p Is Required for Homodimerization and Is Essential for Its E1 Activity and E1-

E2 Complex Formation," The Journal of Cell Biology 276, no. 13 (2001): 9846–9854, 10.1074/jbc.M007737200.

27. Kelley LA, Mezulis S, Yates CM, Wass MN, and Sternberg MJE, "The Phyre2 Web Portal for Protein Modeling, Prediction and Analysis," Nature Protocols 10, no. 6 (2015): 845–858, 10.1038/nprot.2015.053. [PubMed: 25950237]
28. Noda NN, Satoo K, Fujioka Y, et al. , "Structural Basis of Atg8 Activation by a Homodimeric E1, Atg7," Molecular Cell 44, no. 3 (2011): 462–475, 10.1016/j.molcel.2011.08.035. [PubMed: 22055191]
29. Kaiser SE, Qiu Y, Coats JE, Mao K, Klionsky DJ, and Schulman BA, "Structures of Atg7-Atg3 and Atg7-Atg10 Reveal Noncanonical Mechanisms of E2 Recruitment by the Autophagy E1," Autophagy 9, no. 5 (2013): 778–780, 10.4161/auto.23644. [PubMed: 23388412]
30. Tanida I, Yamasaki M, Komatsu M, and Ueno T, "The FAP Motif Within Human ATG7, an Autophagy-Related E1-Like Enzyme, Is Essential for the E2-Substrate Reaction of LC3 Lipidation," Autophagy 8, no. 1 (2012): 88–97, 10.4161/auto.8.1.18339. [PubMed: 22170151]
31. Li X-B, Gu J-D, and Zhou Q-H, "Review of Aerobic Glycolysis and Its Key Enzymes —New Targets for Lung Cancer Therapy," Thoracic Cancer 6, no. 1 (2015): 17–24, 10.1111/1759-7714.12148. [PubMed: 26273330]
32. Tong M, Saito T, Zhai P, et al. , "Mitophagy Is Essential for Maintaining Cardiac Function During High Fat Diet-Induced Diabetic Cardiomyopathy," Circulation Research 124, no. 9 (2019): 1360–1371, 10.1161/circresaha.118.314607. [PubMed: 30786833]
33. Lo Verso F, Carnio S, Vainshtein A, and Sandri M, "Autophagy Is Not Required to Sustain Exercise and PRKAA1/AMPK Activity but Is Important to Prevent Mitochondrial Damage During Physical Activity," Autophagy 10, no. 11 (2014): 1883–1894, 10.4161/auto.32154. [PubMed: 25483961]
34. Karvela M, Baquero P, Kuntz EM, et al. , "ATG7 Regulates Energy Metabolism, Differentiation and Survival of Philadelphia-Chromosome-Positive Cells," Autophagy 12, no. 6 (2016): 936–948, 10.1080/15548627.2016.1162359. [PubMed: 27168493]
35. Jiao L, Zhang H-L, Li D-D, et al. , "Regulation of Glycolytic Metabolism by Autophagy in Liver Cancer Involves Selective Autophagic Degradation of HK2 (Hexokinase 2)," Autophagy 14, no. 4 (2018): 671–684, 10.1080/15548627.2017.1381804. [PubMed: 28980855]
36. Feng Y, Liu J, Guo W, et al. ., "Atg7 Inhibits Warburg Effect by Suppressing PKM2 Phosphorylation Resulting Reduced Epithelial-Mesenchymal Transition," International Journal of Biological Sciences 14, no. 7 (2018): 775–783, 10.7150/ijbs.26077. [PubMed: 29910687]
37. Lee IH, Cao L, Mostoslavsky R, et al. , "A Role for the NAD-Dependent Deacetylase Sirt1 in the Regulation of Autophagy," Proceedings of the National Academy of Sciences of the United States of America 105, no. 9 (2008): 3374–3379, 10.1073/pnas.0712145105. [PubMed: 18296641]
38. de la Cruz-López KG, Castro-Muñoz LJ, Reyes-Hernández DO, García-Carrancá A, and Manzo-Merino J, "Lactate in the Regulation of Tumor Microenvironment and Therapeutic Approaches," Frontiers in Oncology 9 (2019): 1143, 10.3389/fonc.2019.01143. [PubMed: 31737570]
39. Xia H-G, Najafov A, Geng J, et al. , "Degradation of HK2 by Chaperone-Mediated Autophagy Promotes Metabolic Catastrophe and Cell Death," Journal of Cell Biology 210, no. 5 (2015): 705–716, 10.1083/jcb.201503044. [PubMed: 26323688]
40. González-Rodríguez P, Klionsky DJ, and Joseph B, "Autophagy Regulation by RNA Alternative Splicing and Implications in Human Diseases," Nature Communications 13, no. 1 (2022): 2735, 10.1038/s41467-022-30433-1.
41. Park SM, Ou J, Chamberlain L, et al. , "U2AF35(S34F) Promotes Transformation by Directing Aberrant ATG7 Pre-mRNA 3′ End Formation," Molecular Cell 62, no. 4 (2016): 479–490, 10.1016/j.molcel.2016.04.011. [PubMed: 27184077]
42. Goldman MJ, Craft B, Hastie M, et al. , "Visualizing and Interpreting Cancer Genomics Data via the Xena Platform," Nature Biotechnology 38, no. 6 (June 2020): 675–678, 10.1038/s41587-020-0546-8.
43. Jürgen Cox MM, "MaxQuant Enables High Peptide Identification Rates, Individualized p.p.b.-Range Mass Accuracies and Proteome-Wide Protein Quantification," Nature Biotechnology 26 (2008): 1367–1372.

44. Meena Choi C-YC, Clough T, Broudy D, Killeen T, MacLean B, and Vitek O, “MSstats: An R Package for Statistical Analysis of Quantitative Mass Spectrometry-Based Proteomic Experiments,” Bioinformatics 30 (2014): 2524–2526. [PubMed: 24794931]

45. Vizcaíno JA, Deutsch EW, Wang R, et al. , “ProteomeXchange Provides Globally Coordinated Proteomics Data Submission and Dissemination,” Nature Biotechnology 32, no. 3 (2014): 223–226, 10.1038/nbt.2839.

46. Yasset Perez-Riverol AC, Bai J, Bernal-Llinares M, et al. , “The PRIDE Database and Related Tools and Resources in 2019: Improving Support for Quantification Data,” Nucleic Acids Research 47, no. D1 (2019): D442–D450. [PubMed: 30395289]

47. Shannon AM, Ozier O, Baliga NS, et al. , “Cytoscape: A Software Environment for Integrated Models of Biomolecular Interaction Networks,” Genome Research 13 (2003): 2498–2504. [PubMed: 14597658]

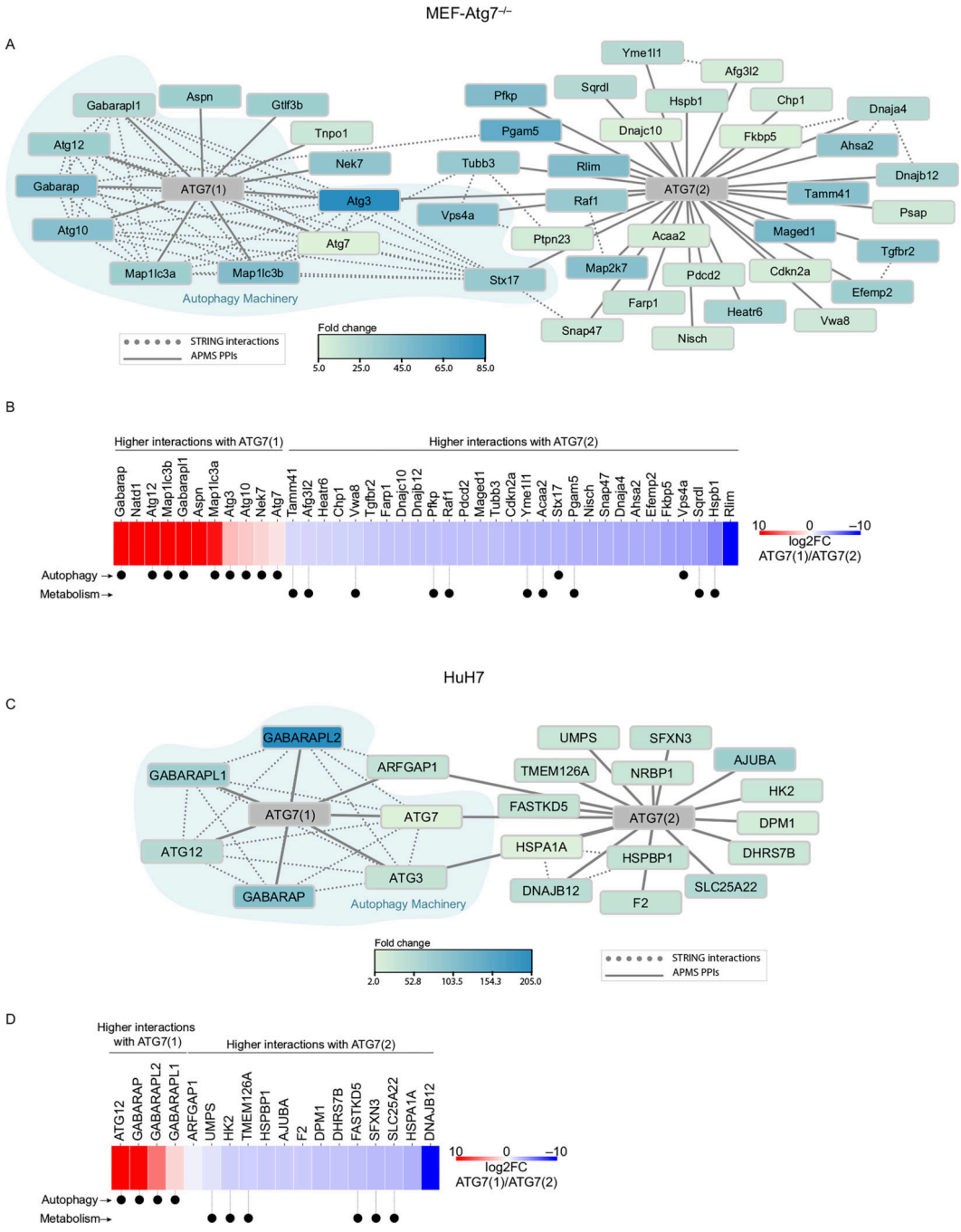

FIGURE 1 |.

ATG7(2) interacts with metabolic proteins and does not interact with core autophagy machinery proteins. (A and C) APMS of the FLAG-tagged ATG7 isoforms in MEF-*Atg7*$^{-/-}$ (A) and in HuH7 cells (C). Interactions detected from these APMS experiments are displayed in the solid line, whereas dotted lines between these proteins are physical interactions from the STRING database. The abundance of individual proteins as compared to the negative control experiments in which ATG7 was not expressed is represented by the colored fold change. (B and D) Representation of all the significant interactions between

ATG7(1) and ATG7(2) in MEF-*Atg7*$^{-/-}$ (B) and in HuH7 cells (D). In red are represented the proteins with higher interaction to ATG7(1) and in blue to ATG7(2). The experiment was performed in MEF-*Atg7*$^{-/-}$ cells.

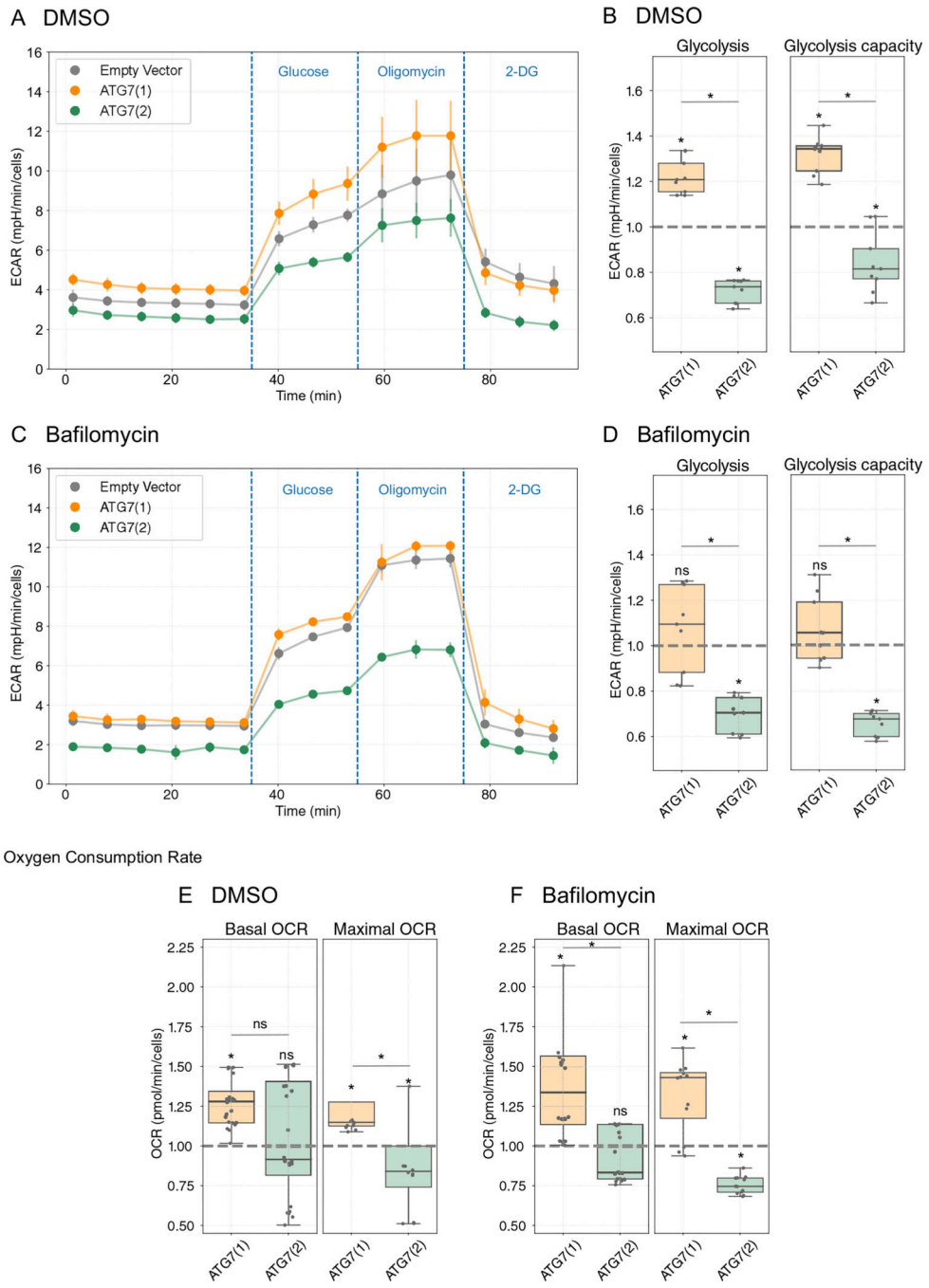

FIGURE 2 |.

ATG7(2) represses glycolysis and mitochondrial activities. (A–D) Extracellular acidification rate (ECAR). Inhibitor injection of 1 mM glucose, 1 μM oligomycin, and 1 mM 2-deoxy-d-glucose. (A and B) Four hours of DMSO treatment. (A) Representation of one experiment. (B) Glycolysis and maximal glycolysis capacity of three independent experiments. (C and D) Four hours of 100 nM bafilomycin treatment. (C) Representation of one experiment. (D) Glycolysis and maximal glycolysis capacity of three independent experiments. (E and F) Oxygen consumption rate (OCR). Inhibitor injection of 1 mM oligomycin, 1.5 μM FCCP,

and 1 mM rotenone and antimycin A mix. Representation of the basal and maximal OCR rates. (E) After 4 h of DMSO treatment ($n = 4$). (F) After 4 h of bafilomycin treatment ($n = 4$ for maximal OCR and $n = 3$ for basal OCR). Values were normalized on cell number. Each condition was in sextuplicate. Values are relative to EV, which is represented by the dotted lines. Statistical analyses were performed to compare each isoform with the control (EV) and to compare the two isoforms with each other. Mann–Whitney U test; $p < 0.05$. The experiments were performed in MEF-*Atg7*$^{-/-}$ cells.

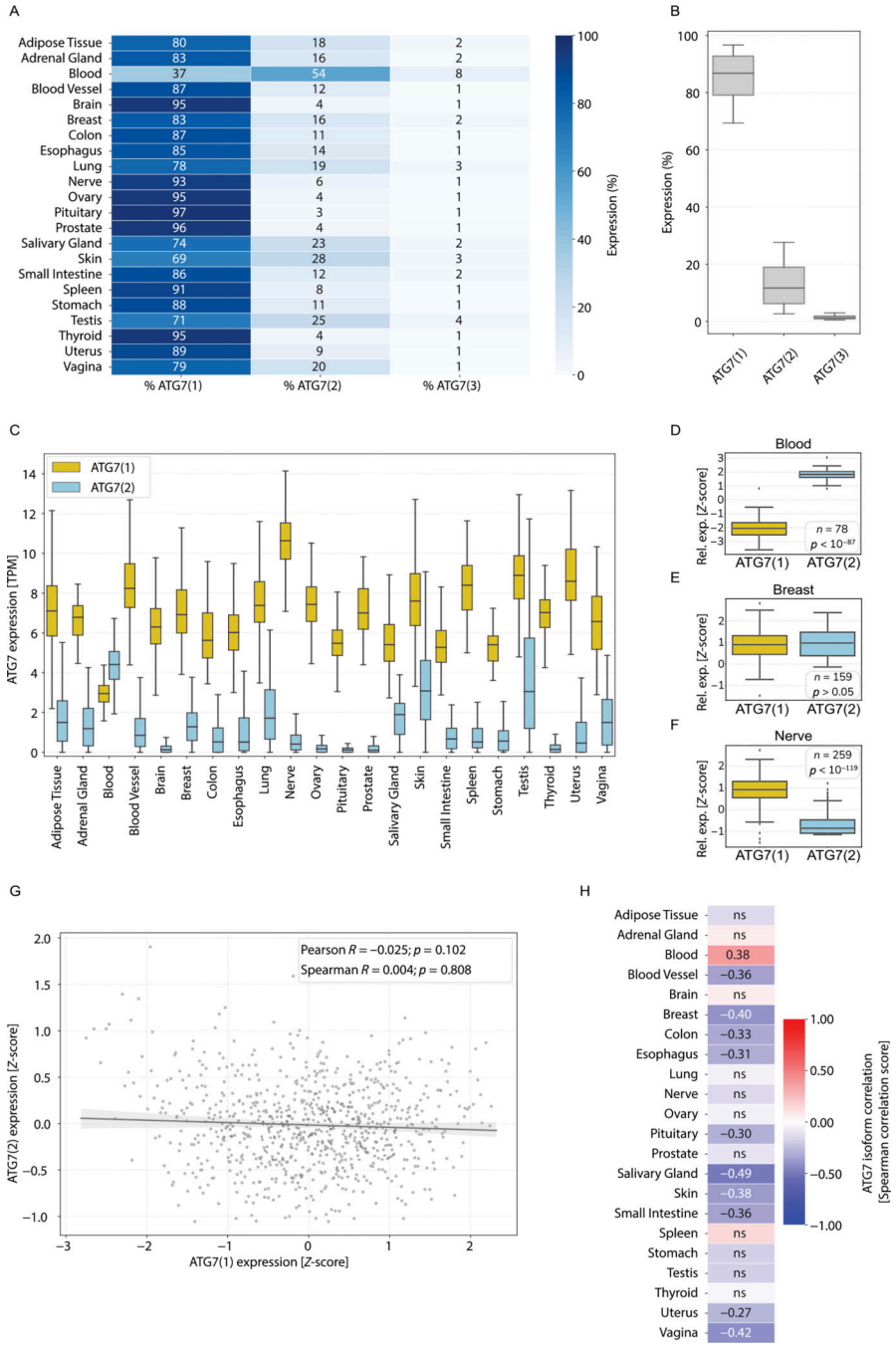

FIGURE 3 |.

ATG7(1) and *ATG7(2)* are not correlated in expression. (A–H) *ATG7* protein coding expression across 22 human tissues from samples registered in GTEx ($n = 4385$). (A and B) Percentage of expression of the three protein coding isoforms of *ATG7* per tissue (A) and in all the 22 tissues (B). (C) *ATG7(1)* and *ATG7(2)* expression. (D–F) Relative expression of *ATG7(1)* and *ATG7(2)* in blood (D), breast (E), and nerve (F); Mann–Whitney *U* test with Bonferroni correction; * is $p < 0.05$. (G and H) Expression correlation of the two isoforms of *ATG7*. (G) Pearson and Spearman correlation between *ATG7(1)* and *ATG7(2)* in all the 22

tissues; bins = 800 to represent $n = 4385$. (H) Spearman rank correlation between *ATG7(1)* and *ATG7(2)* in each tissue; Bonferroni correction; * is $p < 0.05$; correlation threshold at $R > 0.5$ or $R < -0.5$.

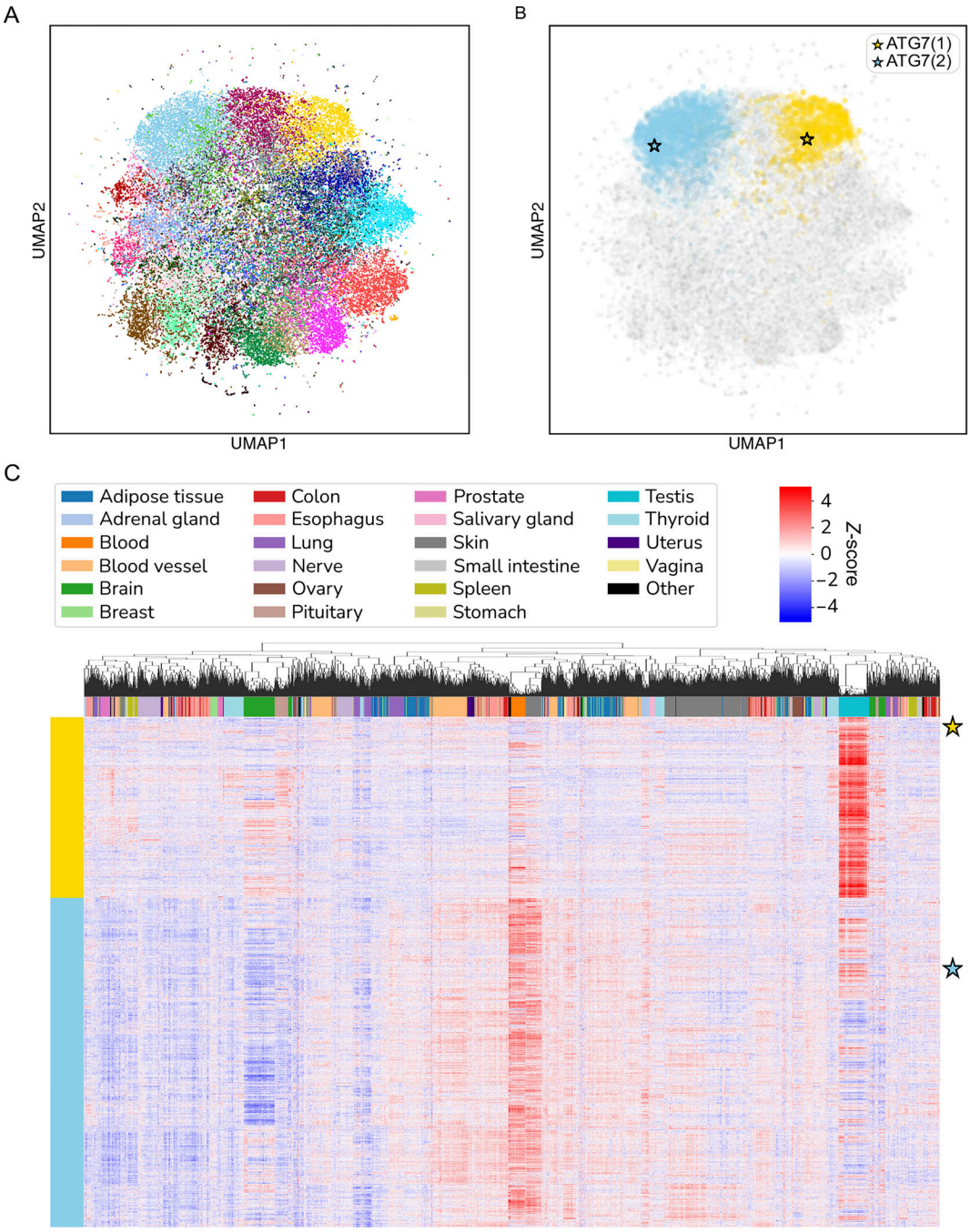

FIGURE 4 |.

ATG7(1) and *ATG7(2)* expressions diverge across human tissues. (A and B) UMAP dimensionality reduction of all transcript's expression (n = 46 490) across samples from GTEx (n = 4385). (A) Colors map to the 168 clusters detected by Leiden clustering (Scanpy implementation of Leiden algorithm). (B) Clusters containing *ATG7(1)* and *ATG7(2)* (in gold and sky-blue color, respectively) are highlighted. Stars indicate the location of each isoform. (C) Relative expression heat map of transcripts included in the two clusters

containing *ATG7(1)* and *ATG7(2)* across human tissues. Stars indicate the location of each isoform; 6598 transcripts across 4385 tissue samples are shown in the heat map.

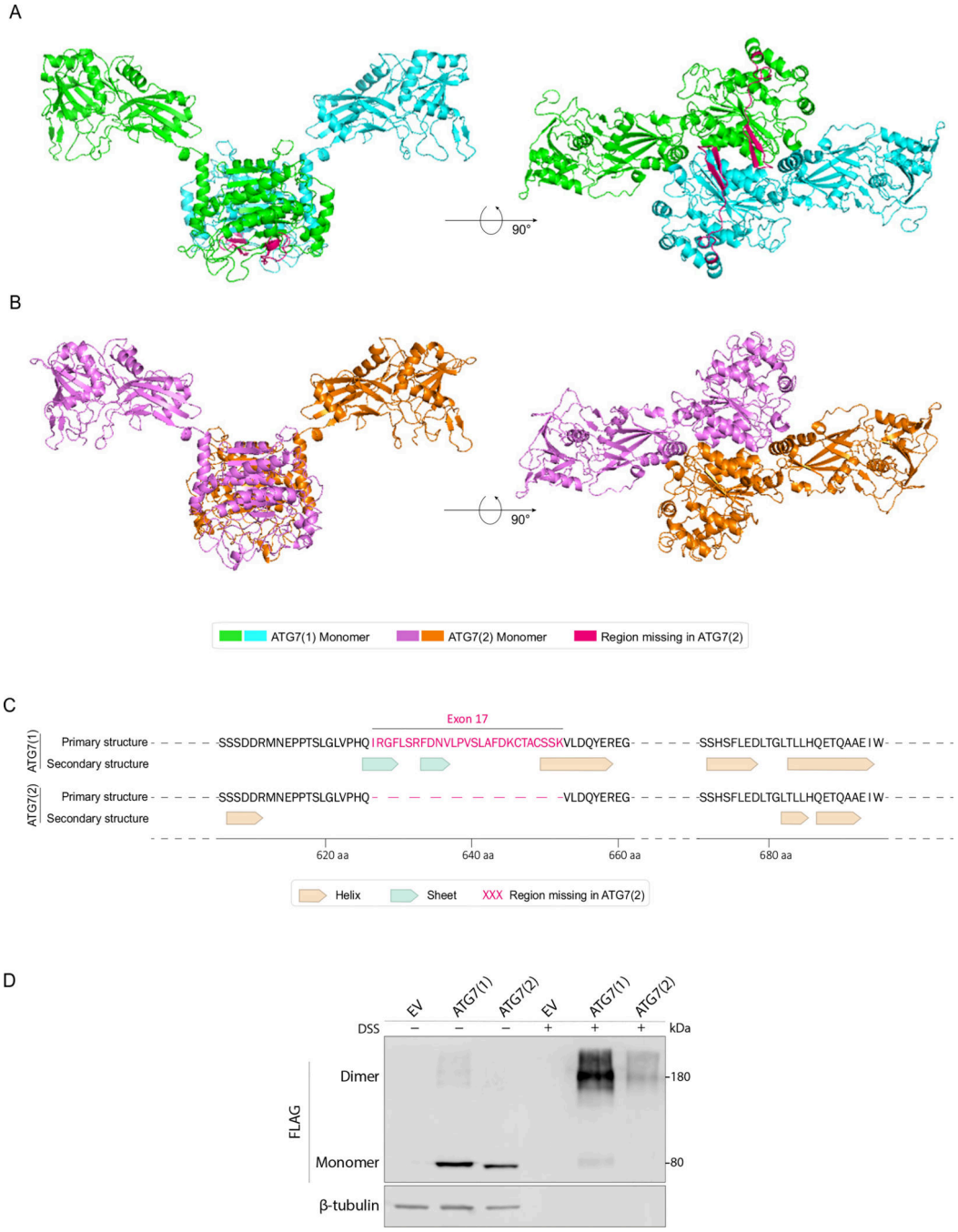

FIGURE 5 |.

ATG7(1) and ATG7(2) structural models are distinct. (A and B) Prediction of human ATG7 dimerization using COTH. (A) ATG7(1) homodimerization. Missing region highlighted in red. (B) ATG7(2) homodimerization. (C) Sequence alignment of the C-terminal region of ATG7(1) and ATG7(2) showing the differences in secondary structure. (D) ATG7 homodimerization analyzed by western blot in MEF-*Atg7*$^{-/-}$ cell lysates cross-linked with disuccinimidyl suberate (DSS).